



Revealing recent calving activity of a tidewater glacier with terrestrial LiDAR reflection intensity

Julian Podgórski^{a,*}, Michał Pęćlicki^{b,1}, Christophe Kinnard^c

^a Institute of Geophysics, Polish Academy of Sciences, ul. Księcia Janusza 64, 01-459 Warsaw, Poland

^b Glaciology Laboratory, Centro de Estudios Científicos (CECs), Arturo Prat 514, Valdivia, Chile

^c Université du Québec à Trois-Rivières, 3351, boul. des Forges, C.P. 500, Trois-Rivières, Québec G9A 5H7, Canada

ARTICLE INFO

Keywords:

LiDAR
LiDAR intensity
Tidewater glacier
Calving
South Shetland Islands
Antarctica

ABSTRACT

In this work we propose a method of estimating the age of calving events of a tidewater glacier based on 3D point clouds. Terrestrial LiDAR scans of the calving front of Fuerza Aerea Glacier (Greenwich Island, South Shetland Islands, Antarctica) were analyzed to determine the timing of the ice face exposure by calving events. Median reflection intensity of laser beam within a calving event footprint (I) was shown to be the best proxy measure of the ice exposure time (t_{LC}). Point clouds were used in concert with information about calving location to create a mathematical model of the intensity-time relationship. An exponential function in the form of $I = a \cdot \exp(b/t_{LC}) + c$ has been shown to describe the relationship between median reflection intensity and time elapsed since the last calving event in a given part of the glacier. The model explains over 60% of the variability in reflection intensity between calving events. The shape of the model curve limits the prediction capability to events occurring up to 3 days before a scan. Development of weathered or superimposed ice on the calving scars is proposed as the explanation for increase of ice reflectivity with time.

1. Introduction

Calving is an important mode of ice loss of water-terminating glaciers. Glacial meltwater is an important contributor to the sea level rise (Gardner et al., 2013), threatening coastal zones all over the world (Dasgupta et al., 2009; Katsman et al., 2011). It is estimated that up to 45% of Antarctic (Rignot et al., 2013) and around 50% of Greenland (van den Broeke et al., 2009) Ice Sheet ice loss can be attributed to calving.

Glaciers and ice caps (GIC) are a class of small ice bodies found both in the polar regions and outside them. A large number of GIC terminate and calve into the ocean, particularly those located in Alaska, the High Arctic, the Antarctic and Patagonia. Although GIC represent only a small fraction of the global ice mass, their contribution to sea level rise is comparable to that of the Greenland Ice Sheet (Vaughan et al., 2013; van den Broeke et al., 2016). It is predicted that GIC will contribute no more than 20 cm of sea level rise until 2100, out of 131 cm (at most) predicted under the most pessimistic climate change scenario (Slangen

et al., 2016). At the regional scale, calving of tidewater glaciers was predicted to produce up to 75% of sea level rise in the Antarctic Peninsula (AP) area, depending on the warming scenario, which may impact ice shelves in the area (Schannwell et al., 2016).

The Arctic and the Southern Oceans are sites of increasing human activity in the recent years (Tin et al., 2009). This rise stems from the steady influx of tourists (Bender et al., 2016) and researchers as well as from increased economic activity, such as shipping (Eguíluz et al., 2016) or resource extraction (Dhargalkar and Verlecar, 2009). Increased human presence requires more robust safety precautions. Growlers and icebergs are seen as one of the greatest risks for shipping in the Arctic region (Lasserre et al., 2016). These floating pieces of ice are a direct product of glaciers calving to the sea. Precise knowledge of the time and size of calving events is thus necessary to model the spread of growlers and icebergs that could affect marine traffic.

Both ecological and economic reasons justify research efforts devoted to understanding glacial calving mechanisms. While topics such as calving rates (Dowdeswell et al., 2008; Luckman et al., 2015) or GIC

Abbreviations: AC, Analysed Cloud; AIC, Akaike Information Criterion; ALS, Airborne Laser Scanning; AP, Antarctic Peninsula; CP, Control Point; DEM, Digital Elevation Model; E, Nash-Sutcliffe indicator of model prediction efficiency; GIC, Glaciers and Ice Caps; GLIMS, Glacier and Land Ice Monitoring from Space; GoF, goodness of fit; I , reflection intensity; IR, Infrared; LiDAR, Light Detection and Ranging; LOO, Leave-One-Out; PDF, Probability Distribution Function; RC, Reference Cloud; RMSE, Root Mean Square Error; RSS, sum of squares of residuals; SEM, Standard Error of Mean; SSI, South Shetland Islands; t_{LC} , time since the last calving event; TLS, Terrestrial Laser Scanning

* Corresponding author.

E-mail addresses: jpodgo@igf.edu.pl (J. Podgórski), michal@cecs.cl (M. Pęćlicki), christophe.kinnard@uqtr.ca (C. Kinnard).

¹ These authors contributed equally to this work.

<https://doi.org/10.1016/j.coldregions.2018.03.003>

Received 12 August 2017; Received in revised form 23 January 2018; Accepted 4 March 2018

Available online 14 March 2018

0165-232X/ © 2018 Elsevier B.V. All rights reserved.

calving dynamics (Sakakibara and Sugiyama, 2014) are frequently covered in the literature, studies of ice cliffs during or shortly after a calving event are still scarce and mostly restricted to Greenland outlet glaciers (Holland et al., 2016; Lüthi and Vieli, 2016; Xie et al., 2016). This stems from the high cost of conducting fieldwork in the vicinity of a calving front which explains the comparatively small amount of studies. Recently, various emerging technologies such as Unmanned Aerial Vehicles (Ryan et al., 2015) or underwater acoustic monitoring (Glowacki et al., 2015) have been employed in ice cliff studies. Among these, the Light Detection and Ranging (LiDAR) surveying method allows for precise measurements of the optical and geometrical properties of an ice wall, thus enabling in-depth studies of calving events.

LiDAR technologies are nowadays popular in cryospheric research. Bhardwaj et al. (2016) list a number of studies such as works of Petrich et al. (2012), Jóhannesson et al. (2013), and Moeser et al. (2015) employing LiDAR in various ways. The technology is used when detailed, 3-dimensional models of glaciers are needed, for example for mapping (Hopkinson et al., 2001; Pętllicki et al., 2017), volumetric assessment of glacial phenomena (Pętllicki and Kinnard, 2016) or mass balance studies (Kääb et al., 2012; Gabbud et al., 2015; Fischer et al., 2016). Terrestrial Laser Scanning (TLS) found its use in glacial geomorphology (Carrivick et al., 2013; Kociuba et al., 2014) and was also used to measure sea ice roughness (Landy et al., 2015). Studies were conducted not only in the polar areas, but also in the Alps (Roncat et al., 2013; Carrivick et al., 2013), North America (Hopkinson et al., 2012) and Spain (De Sanjosé et al., 2014).

The information acquired with LiDAR is also used alongside other datasets. Airborne Laser Scanning (ALS)-based digital elevation models (DEM) can be coupled with thermal imagery (Hopkinson et al., 2010) to identify ice-cored moraines or used within a geographical information system for snow cover depth assessment (Hopkinson et al., 2012). Such DEMs were also employed to validate snow depth information acquired from field-based sensors (Kerkez et al., 2012).

While the laser time-of-flight has been abundantly used to derive high-resolution topographic data, the intensity of the returning laser pulse provided by the LiDAR scanners is a relatively new method of imaging. Within cryospheric sciences it is explored in snow research (Kaasalainen et al., 2008) or for the classification of glacial features (Höfle et al., 2007). Radiometrically calibrated full waveform LiDAR returns were also used for delineating rock glaciers in alpine setting (Roncat et al., 2013).

The rapid development of the LiDAR-related technologies provides Earth scientists with a large amount of high-resolution data covering multiple environmental scales. Integration of these data with information coming from different sources, or devising novel uses for the laser scanned models of the environment are among the most important challenges facing researchers working with LiDAR (Harpold et al., 2015).

In this work we propose a novel method to assess the time elapsed since the last calving event (Time since Last Calving, t_{LC}) across an ice cliff, based on LiDAR scans of the cliff. Changes in the median reflection intensity of a laser beam from the scanned object (I) within a calving event footprint are used to develop and validate a model of the $t_{LC} - I$ relationship.

Although the fieldwork that yielded the datasets was conducted in the South Shetland Islands, Antarctica, the proposed methodology of model development is general. Nevertheless, its use would require preparation for each case of scanning a particular ice body with a particular scanner. Properties of scanned ice surface (e.g. sediment content, roughness) and instrument type influence the output of a model in a way that cannot be accounted for without specific calibration.

Such algorithm would expand the usability of laser scanning in glacier studies beyond 3D volume assessments, as suggested by Eitel et al. (2016). The events visible as volumetric (3D) differences between two point clouds taken at different times could be dated with more

precision than based solely on the time difference between the acquisitions which can overestimate the true time since calving. In theory, the LiDAR scans could thus be used for temporal inventorying of calving events, without having to deploy other equipment such as time-lapse or video cameras. Laser scanning is a technology with well-established commercial and scientific applications and many terminologies describing various factors and phenomena have been proposed. The terminology established by Kashani et al. (2015) will be used throughout this work.

2. Materials and methods

2.1. Study site

Greenwich Island is located in the central part of the South Shetland Islands (SSI) archipelago, at the northern tip of the Antarctic Peninsula (AP). In the second half of the 20th century the region has been subjected to intense warming (Vaughan et al., 2003) which caused extraordinarily strong melting of glaciers (Hock et al., 2009). The climate trend has reversed to cooling at the turn of the century (Turner et al., 2016) resulting in positive surface mass balance among smaller glaciers in the SSI and northern AP (Navarro et al., 2013; Oliva et al., 2017; Pętllicki et al., 2017). Nonetheless, as the retreat of the majority of glaciers in the AP region is driven by an increase in ocean temperature (Cook et al., 2016a), the future evolution of calving rates remains uncertain. With 142 km² of surface area, Greenwich Island is the sixth largest of the eleven major islands in the group. The major feature of Earth science interest on the island are its raised beaches, which were used to infer about Holocene isostatic uplift rates (Fretwell et al., 2010) or Neoglacial ice advance (Simms et al., 2012). The latest glacial advance was dated to AD 1500–1700 (Hall, 2010). The studied glacier, Fuerza Aerea, is an NW-flowing outlet glacier of the Greenwich Island ice cap. Its surface area is 7.2 km², with a length of < 3 km (Bliss et al., 2014). According to the Glacier and Land Ice Monitoring from Space (GLIMS) database it is classified as a retreating glacier without moraines (Rau et al., 2005; Bliss et al., 2014). The classification is in agreement with the general retreat trend of the glaciers in the archipelago (Cook et al., 2005). At the time of data acquisition (Jan–Feb 2013) the ice flow velocity at the front was 0.26 m/d, while calving contributed 0.41 m/d of retreat, with a net frontal retreat of 2.07 m (0.15 m/d) over a two-week study period (Pętllicki and Kinnard, 2016). Fuerza Aerea is a tidewater glacier, terminating in the SE sector of Montecino Cove, an inlet of Discovery Bay, the largest bay of the island. Sotos Island is located in vicinity of the glacier terminus, while Silva Island lies circa 800 m away. The area is home to the Chilean Arturo Prat Antarctic base. Fig. 1 depicts the location of the island as well as the setup of instruments used to measure the glacial front.

2.2. Data acquisition

The work is based on the terrestrial laser scanning (TLS) and video camera dataset acquired during a fieldwork campaign in austral summer 2012/13 (Pętllicki and Kinnard, 2016). An Optech ILRIS-LR terrestrial laser scanner was used to obtain raw point clouds of the calving ice front while a Mobotix MX-M24-M video camera with a 32 mm lens was continuously recording the glacial front over the two-week study period. The camera was placed on Sotos Island. The laser scanner was set on the more distant Silva Island (Fig. 1). The island was chosen because it is the only piece of stable ground providing an unobstructed view over the ice cliff for the scanner. The distance between the scanner and the studied ice wall was approximately 730 m. The scanner uses a class-3 laser operating at a wavelength of 1064 nm and has a maximum operating range of 3000 m. The peak laser repetition rate is 10 kHz, and minimum spacing of individual points is 2 cm at 1000 m of range (OPTECH, 2010). The mean vertical and horizontal spacing of points was approximately 6 cm, with individual values being

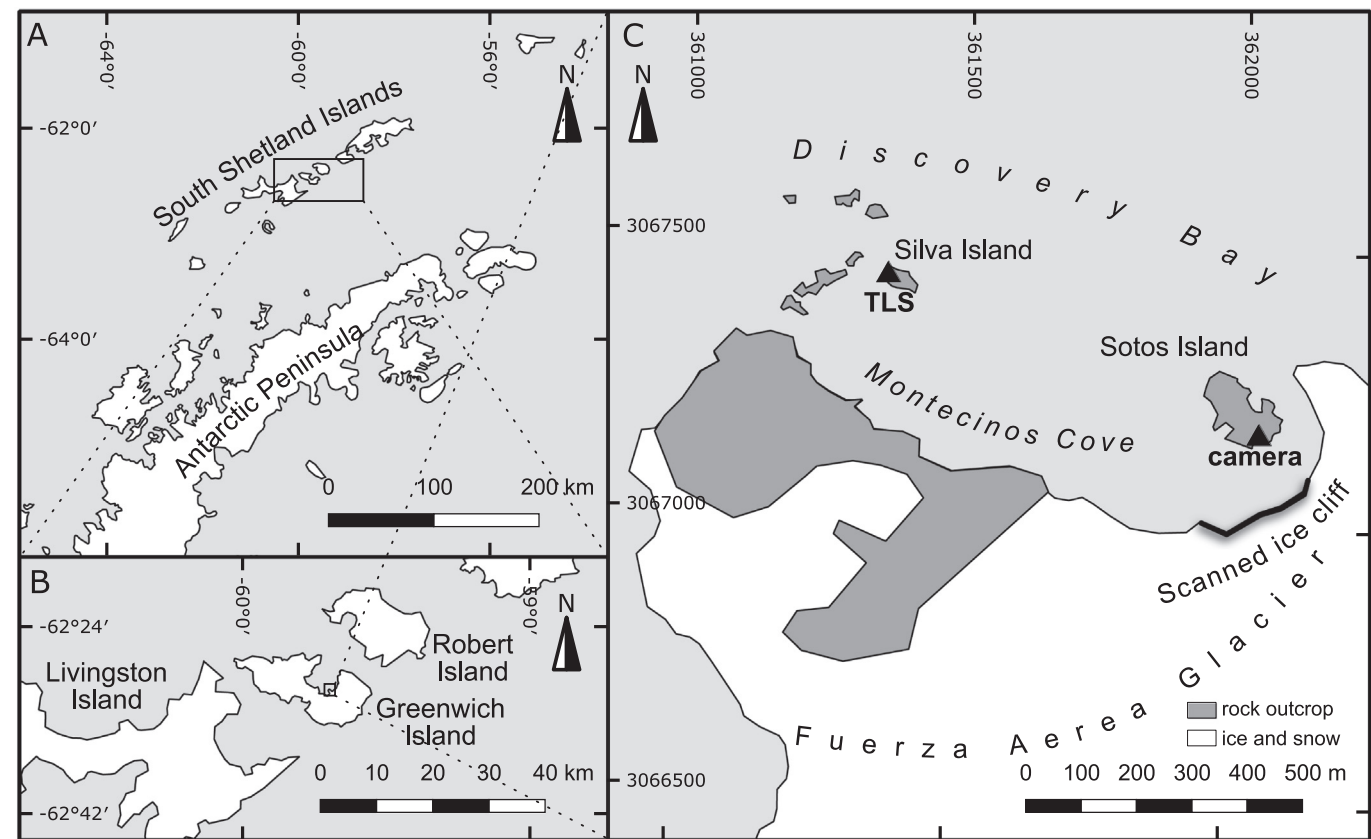


Fig. 1. Location of South Shetland Islands in the Antarctic Peninsula region (A), position of Greenwich Island within the archipelago (B) and the study site (C). The scanned part of the ice cliff is marked in black, as well as location of the terrestrial laser scanner (TLS) and the camera. The coordinates on panel C are expressed in UTM zone 21S coordinate system.

slightly lower or higher depending on the local distance from the scanner. Vector contours of calving scars (calving contours) on the ice front were delineated manually based on frames extracted from the video recording before and after calving occurred. These were georeferenced in a local cartesian coordinate system. Taken together, the TLS and video camera datasets provided precise localization and timing of calving events over a two-week study period.

Five scanning sessions were selected for further processing, based on their quality and distribution in time. The chosen raw point clouds were first converted to an ASCII format, read by the open source point-cloud processing software CloudCompare (CloudCompare, 2017), with use of a dedicated Optech Parser program. The distance error introduced by the varying atmospheric conditions was eliminated at this point using data recorded at a weather station located in the nearby Arturo Prat Chilean Antarctic base. The meteorological data were sampled at 3 h interval. The output was a series of file groups, each consisting of point clouds acquired during a single scanning session. Low-resolution scans, covering the whole ice cliff with surroundings both above and on the sides (Reference Clouds - RCs), were used for coregistration of scanning sessions to each another. High-resolution scans (Analysed Clouds - ACs) encompassed only the studied section of the ice wall, without many markers usable for georegistration.

2.3. Geometric preprocessing

The second step of preprocessing was the co-registration of the point clouds to achieve spatial correspondence between scans. The parsed outputs were not georeferenced.

The points had coordinates in an arbitrary system with origin at the scanner's location. The coordinate systems of each scanning session were thus independent of each another, but expressed in the same units

(meters from the scanner's position). To allow for comparison of corresponding parts of the ice cliff the point clouds were co-registered that is, their coordinates were recalculated to a common coordinate system, ensuring overlap of the cliff images. The intensity values were unaltered by the registration process.

A single RC from an early scanning session covering the widest fragment of the ice front was chosen as the reference to which other RCs were coregistered. The RCs representing all further scanning sessions were registered to this reference cloud using a set of common control points (CP), picked manually on each point cloud. Control points (CP) within the point clouds were selected in areas assumed to have remained stable over the course of the study, such as rocky outcrops. The registration parameters, i.e. the translation/rotation matrix and the scale factor, were generated from each RC's registration and saved. These values were used to transform the denser, but narrower, ACs to a common coordinate system. The ACs do not contain CPs that would be stable over the whole period of measurement campaign, as they include only ice.

The point cloud registration errors (Root Mean Square Error - RMSE) were calculated automatically by CloudCompare during alignment of the RCs. At this stage the values never exceeded 1 m, and were most often around or below 0.5 m (Table 1). The purpose of this step was to bring all scans to a common coordinate system, within which a

Table 1
Dates of LiDAR scans used in the study, RMSE of first stage of registration of RCs.

Scan date	26.01.2013	31.01.2013	01.02.2013	02.02.2013	04.02.2013
RMSE (m)	0.53	0.18	0.94	0.40	0.51

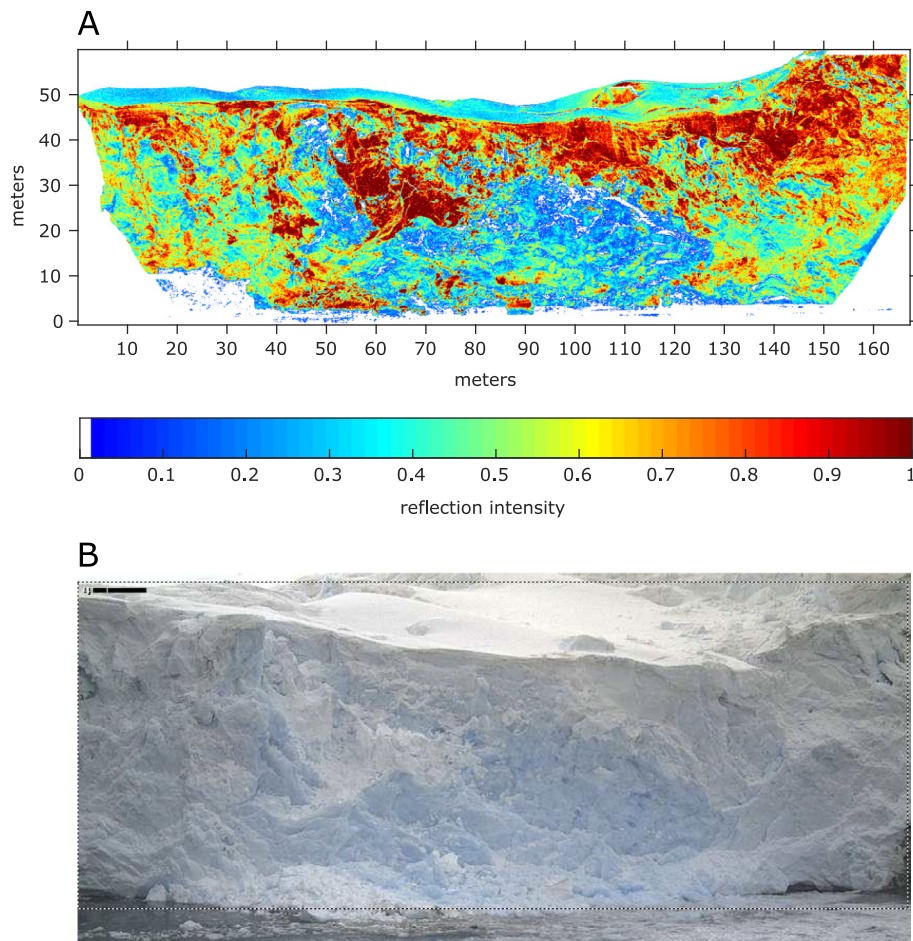


Fig. 2. A LiDAR scan includes the intensity of reflected radiation in the returned data. A scan with only atmospheric correction applied is shown on panel A, cropped to the extent of the studied ice cliff. Panel B is a photograph from the camera taken roughly at the time of the scan.

finer registration of ACs exclusively was done. The ACs coregistered with parameters derived from RCs were still displaced to a degree potentially influencing the final result.

The same CP-picking method was assumed using ACs exclusively to improve overlap of ACs. In absence of rocks, or similar constant points, features of ice cliffs (cracks, protrusions) which did not change between two subsequent scans were picked as CPs. The sets of these points were different for each AC, as the evolution of ice wall removed CPs available for the early scans and created new, stable only in the later time. This operation improved the fit between ice cliffs. Measurement of quality of registration of ACs by means of point-cloud-wide calculation of displacement was not performed. The point-to-point distances are measured in 3-dimensional space. This means that the points located within a calving scar will exhibit large distance to the cloud located temporally before the calving event and bias the results. The error assessment thus obtained would not be meaningful as a measure of quality.

CP-picking was further used to register the shapefiles containing the calving contours to the point clouds. A set of CPs was created in QGIS software based on a photograph of the ice front (similar to the one included on Fig. 2) and the reference point cloud synchronous with the photograph. The shapefiles delineating calving scars on the ice cliff were then exported to a more universal ASCII format. The scale and transformation matrix were used in CloudCompare to register the polygon shapes to the reference system established earlier by the point clouds.

The registered clouds were cropped to cover only the extent of ice cliff included on the camera images. An example of a dataset at this stage is shown on Fig. 2. All further processing stages were done in Matlab software.

2.4. Radiometric calibration of intensity values

A less computationally-efficient ASCII format was used to store and process the point clouds. Files saved in the binary .las format altered the intensity values stored in the files - floating-point values were lost. Solving this problem would require addition of further steps to the cloud processing workflow, which would have little impact on efficiency comparing with ASCII but would introduce possible source of errors.

The reflection intensity of a LiDAR impulse is dependent on a number of factors, the most influential ones being the reflectivity of the scanned ice surface, its roughness, and wetness (Heritage and Large, 2009). These features are those of interest in this study, although it was not possible to separate the respective influence of the different factors on the received signal. The other influential factors were either constant during the study (parameters of the scanner) or were accounted for during preprocessing (weather, distance to the target, incidence angle).

The correction of intensity values for the errors introduced by variations in the angle of incidence of the LiDAR has been shown to improve the accuracy of point cloud datasets in glacial applications (Höfle et al., 2007). It is also required if multi-temporal analyses are to be performed. Calibration of LiDAR intensity which yields intensities dependent only on surface properties of the scanned object is known as absolute calibration (Kaasalainen et al., 2011b). Such absolute calibration was performed in this study using Eq. (1)

$$I_c = I_a \frac{R^2}{R_{ref}^2} \cos^{-1} \alpha \quad (1)$$

where I_c stands for the corrected intensity and I_a represents intensity

values corrected for atmospheric distortion by the dedicated parser program. Two factors are responsible for correction of different effects:

- $\frac{R}{R_{ref}}$ removes the effect of variable distance between the scanner and ice cliff. It is based on the Starek et al. (2006) routine for correction of Airborne Laser Scanning intensity for distance. R is the distance of the corrected point from the scanner, and R_{ref} is a reference distance. The latter was computed as the mean scanner-point distance in the point cloud used for fine co-registration of ACs.
- $\cos^{-1}\alpha$ factor was based on Gross et al. (2008) and removes the influence of incidence angle on the intensity return. The α is the angle between the laser beam and surface normal in the point of contact.

The latter effect is particularly strong when specular surfaces are scanned (Heritage and Large, 2009). Normal vectors were computed in CloudCompare with octree method for each point in a cloud, based on the topography surrounding the point. The area with radius of circa 0.2 to 0.3 m was included as local plane, relative to which the normal was computed. As the clouds were stored and processed in a local coordinate reference system where scanner's position was (0,0,0), the coordinates (X,Y,Z) of each point were equivalent to the coordinates of a vector corresponding to the laser beam direction. Therefore, $\cos\alpha$ was equal to

$$\cos\alpha = \frac{n \cdot l}{|n||l|} \quad (2)$$

where n is the normal vector and l is the laser-beam vector.

The formula in Eq. (1) was built on principles designed for ALS despite being applied to TLS. Terrestrial laser reflection intensity measurements are often troubled by near-distance effects, which cannot be accounted for in a correction methodology devised for ALS. This study however made use of a long-range laser scanner. The distance between the scanning device and the target (ice cliff) was close to 800 m. Near-distance effect studies are concerned with scanner-target distances below 100 m (Fang et al., 2015; Kaasalainen et al., 2011a), while operating altitudes of ALS are in the hundreds-of-meters order (Gallay, 2012). Thus ALS equations have been chosen as more suitable for intensity corrections.

In the final stage of radiometric preprocessing the points that were too bright (with intensity return higher than 0.95) were removed from the datasets. They were assumed to be either erroneous or related to snow. Such operation is warranted by the main focus of this study, i.e. the properties of glacial ice. Information from snow-covered areas was expected to bias the result.

2.5. Development of model

The freshly-exposed glacial ice can be expected to undergo gradual change of reflectivity when subject to factors such as insolation or freeze-thaw cycling. Indeed, such change can be observed with the naked eye, as evidenced on Fig. 2B, where the newly exposed fragment of the ice cliff is visibly more blue than its surroundings, where calvings have occurred much earlier. This work studies the same difference but observed in near-IR (the wavelength of the laser scanner used) and at much greater resolution than achievable with a camera image. It is hypothesized that there exists a mathematical model governing this aging of the ice surface observed with the intensity of reflection of LiDAR scanner pulses from the ice surface. The main effort of the work is thus to determine the relationship expressed as a mathematical function of LiDAR return intensity (I) dependent on the time of last calving (t_{LC}):

$$I = f(t_{LC}) \quad (3)$$

A relationship between albedo and age of snow was proposed before by Oerlemans and Knap (1998) who parameterized snow aging by an

exponential time-decay function. In this study similar model of the reflection intensity change with time was used. The difference between the relationship established for snow and the model proposed in this work is the direction of the change. Snow albedo change follows a decreasing curve as it darkens over time. The model assumed in this study had to emulate increase in reflectivity with time. A formula seen in Eq. (4) was used as the model:

$$I = a \cdot \exp \frac{b}{t_{LC}} + c \quad (4)$$

This equation can be physically interpreted to represent the following model:

$$I = (I_f - I_n) \cdot \exp \frac{t^*}{t_{LC}} + I_n \quad (5)$$

where I_n and I_f represent the intensity values of newly exposed ice surface and that of the final form of aged ice surface, respectively. As such after being exposed to the elements for a certain time, further reworking does not impact the reflectivity significantly and the reflectivity converges towards a typical aged value, I_f . t^* is a characteristic decay time scale.

The values of parameters of Eqs. (4) and (6) were obtained by best-fitting a model to a dataset consisting of t_{LC} - I pairs for each considered calving. The shapefile polygons delineating calving scars were assigned their respective times of event with the accuracy of a minute. Timing of laser scans is known with similar accuracy - the starting moment of the scan was stored with an accuracy of a second while particular points were registered up to around 30 min later, due to the duration of a scan acquisition. It was degraded to minute accuracy to match the calving polygon timing accuracy. With timestamps of LiDAR scans and calving events available it was possible to assign a time from last calving (t_{LC}) value to each point of a cloud. It is defined as the difference between the time of the scan and the latest time at which a calving event occurred in a particular area of the ice cliff.

The initial shapefiles were cropped in order to account for overlapping calvings and to create a map of t_{LC} across the cliff face (Fig. 3). It was saved in the form of a point cloud where the scalar field value of every point was either the t_{LC} , or 0 if a point was not within the footprint of any calving event. This way every scanned point on the ice wall was assigned a value for both variables in Eq. (3). As each laser scan had a different timestamp (resulting in increasing t_{LC} at the location of the same calving event) and new calvings were occurring between the scans (changing the t_{LC} map), the procedure had to be repeated for each point cloud separately. The calving contours used for model fitting were filtered to remove those lying on the edge of the camera field of view. Calving polygons representing fragments of larger events (with the remaining part outside camera field of view) were not comparable with the events overlapping with the point clouds entirely.

Attempts to fit alternate form of the model were made. This version included two exponential terms, as seen in Eq. (6):

$$I = a \cdot \exp \frac{b}{t_{LC}} + c \cdot \exp \frac{d}{t_{LC}} + e \quad (6)$$

It has, however, failed to perform in a satisfactory way. Most importantly, it was impossible to establish a good fit of the model. The number of points to which the functions was fitted was too low to provide a reliable fit of a function with 5 coefficients. The bounds of prediction were very high and the fitted coefficients were not statistically significant. The values of the coefficients and shapes of the model functions were suggesting that the two-term equation was only approximating the single-term one.

2.6. Generalization of intensity signal

The intensity signal displayed considerable spatial variability within each individual calving polygon despite the applied corrections.

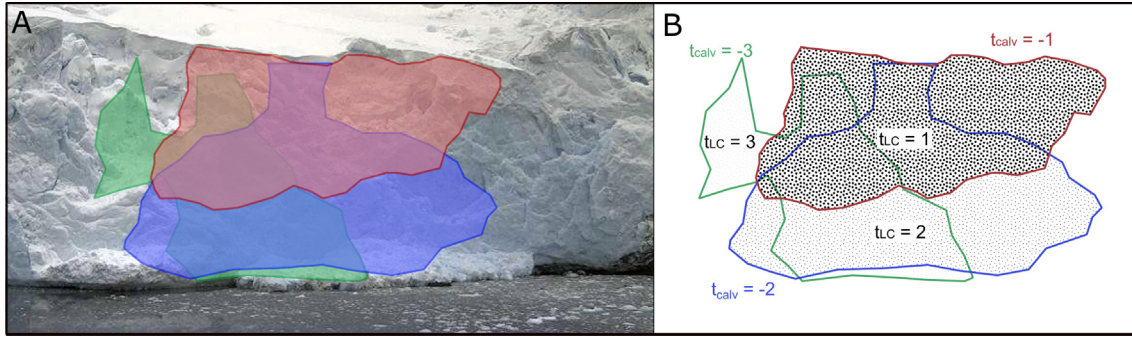


Fig. 3. Cropping calving contours with one another is necessary to accurately map t_{LC} , as for example a more recent calving event superimposed onto an earlier one would reduce the mapped area with a longer t_{LC} . Panel A shows overlap of calving footprints on the background of a photographed ice wall. Panel B shows the relationships between the 3 differently timed events: t_{calv} marks the day, on which a calving event occurred (1st, 2nd, or 3rd day before present) and relates to the colored outlines. Patterns differentiate areas of different t_{LC} - which may overlap and thus not be identical to contours of particular calving event. The denser patterns represent lower t_{LC} , produced by later calving events. (For interpretation of the references to color in this figure legend, the reader is referred to the web version of this article.)

Therefore it was necessary to use statistical measures to assign generalized I values to t_{LC} of each calving contour. Four statistical measures were considered as indicators of central tendency for the LiDAR intensity of each calving polygon:

1. Mean of intensities of all points within a calving polygon. In this case Standard Error of Mean (SEM) was computed to assess suitability of data for fitting. The formula used was

$$SEM = \frac{\sigma(S)}{\sqrt{N^* - 1}} \quad (7)$$

with σ standing for the standard deviation, S for sample (intensities of points within a polygon in this case) and N^* for the effective sample size. The latter was used instead of the true sample size N , i.e. the number of points within a calving polygon, as the data in this study can be considered as spatially autocorrelated. Therefore, the effective sample size should be lower than N . A semivariogram was calculated for each calving event and a theoretical semivariogram model was fitted with use of exponential fitting method. A formula devised by Griffith (2005) for spatially autocorrelated data was used to compute the N^* :

$$1 + \frac{N - 1}{1 + 51.4879 \left(\frac{r}{d_{max}} \right)^{1.7576}} \quad (8)$$

where r is the range parameter of the fitted semi-variogram and d_{max} - highest distance between points in the dataset. As seen on Fig. 7 the SEM are very low, owing to the large number of points (samples) within each calving polygon. The highest value of SEM in the dataset was 0.0044.

2. Median of intensities of all points within a calving polygon. The median is often a better predictor of central tendency than mean when skewed distributions are considered.
3. Mode of histogram of intensities. Mode of histogram of intensities within a calving polygon was adopted as an approximation of the mode of the set of points. Histograms were formed with bin size of 0.05 and the value corresponding to the highest bin was used as an approximation of the mode of the I set.
4. Mode of a fitted Beta probability density function (PDF). A theoretical probability density function was fitted to the I histograms in order to track the shifting center of mass of the distributions. Beta PDF (Gupta, 2011) was chosen to best represent the type of data at hand. The Beta distribution is a family of continuous probability distributions defined on the interval $[0, 1]$ parametrized by two positive shape parameters, denoted by α and β , and which accommodate varying distribution shape (skewness) (Gupta, 2011):

$$X \sim \text{Beta} \Rightarrow f_X(x) = \frac{1}{B(\alpha, \beta)} \cdot x^{\alpha-1} \cdot (1-x)^{\beta-1}, 0 < x < 1, \alpha, \beta > 0 \quad (9)$$

where

$$B(\alpha, \beta) = \int_0^1 a^{\alpha-1} (1-a)^{\beta-1} da \quad (10)$$

The Beta distribution was fitted to each I histogram using maximum likelihood method. The mode of the fitted, theoretical, PDFs served as the fourth indicator.

The final dataset consisted of a 5-column table, with a set of t_{LC} and values of the aforementioned measures for each calving contour. This table was used as a training and validation dataset in order to determine the most efficient parameter and to find the best parameters for Eqs. (4) and (6).

2.7. Validation of model

K-fold cross-validation (CV) has been performed to assess how well can the models predict t_{LC} of an independent event. The procedure simulated the real-life scenario of assessment of calving dates based on information from previous scans. Five iterations of the procedure were done. Each of them involved training the models on data points derived from four LiDAR scans and using the points from the fifth as verification data, whose t_{LC} was then estimated using the fitted models. The procedure was repeated for the whole dataset (all calving events larger than 100 m²) and the cases limited by the criterion of observed $t_{LC} < 4$.

The results, i.e. modeled t_{LC} , were compared to their respective observed t_{LC} . Statistical measures were used to assess the prediction potential. Data points which could not be predicted by the model (i.e. averaged intensities higher than the limit of the fitted function, which give an infinite t_{LC}) were discarded at this stage. Two indicators related to these data were used: RMSE of the predictions relative to the observations and Nash-Sutcliffe indicator of model prediction efficiency E (Nash and Sutcliffe, 1970).

3. Results

3.1. Reflection intensity distribution within calving polygons

The intensity data in each of the point clouds are very noisy, despite the applied corrections. Histograms of intensity do not show regularity in intensity returns of freshly-exposed areas (Fig. 4). Some of the distributions show visible peaks at expected lower intensities, while others show a distribution similar to that of the entire point cloud. None of the

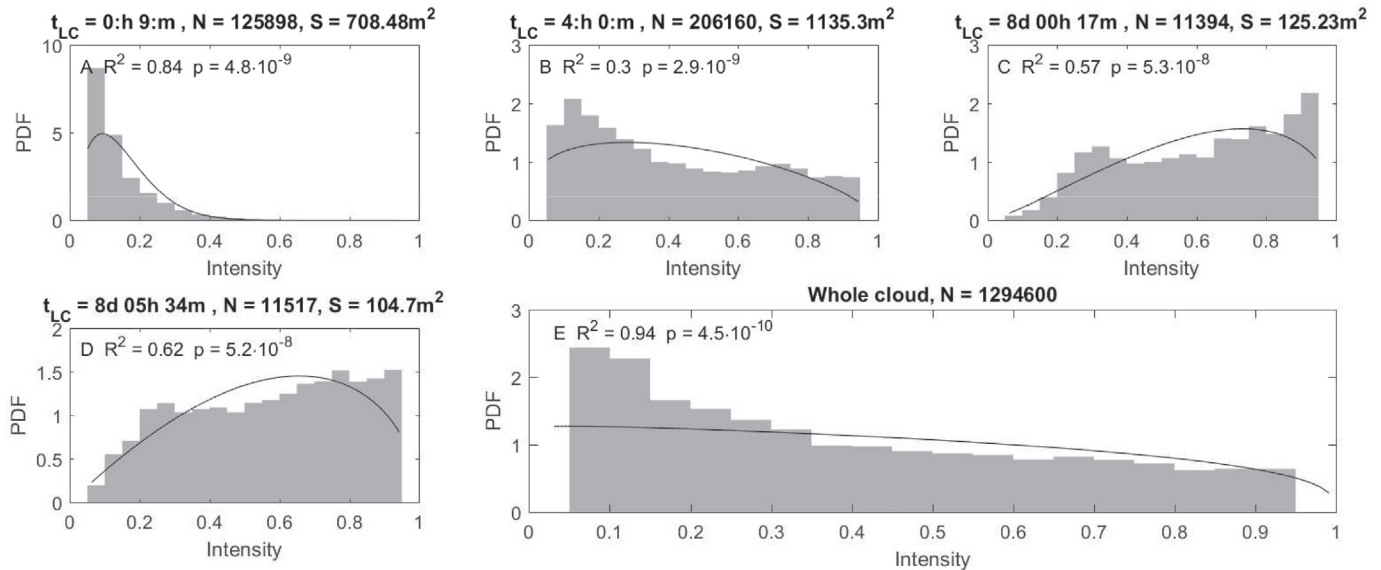


Fig. 4. Histograms of reflection intensity within calving polygons and for a whole point cloud. Intensity is on X axis, the Y axis represents the number of returns normalized for PDF visualization. Each histogram of a calving polygon is described by its observed t_{LC} , number of points included (N) and size in square meters (S). Black lines are beta distributions fitted to the data with the maximum likelihood method. The “Whole cloud” histogram represents the scan taken on 2 Feb 2013, while the histograms of calvings include points within the contours of specific calving events mapped on the whole cloud.

calving polygons contains homogeneous values.

Examples of fitted Beta PDFs along with their 90% confidence intervals are presented on Fig. 4. The coefficient of determination (R^2) values were calculated by checking the correspondence of observed and modeled histogram bin heights. p-Values reported were obtained with the Anderson-Darling goodness of fit (GoF) test (Anderson and Darling, 1954). It was proven to perform best in assessment of Beta distribution fitness when compared to other popular distribution tests by Raschke (2011).

The extremely low p-values show that it is not possible to reliably assess the quality of fit of the distribution to the data. Very large sample sizes made it impossible to reliably assess the goodness of fit of the Beta PDFs. The measures of distribution fit, such as χ -squared test or Anderson-Darling test, are very sensitive to even small inconsistencies between the sample histogram and the PDF fitted to it. The I values are also highly spatially autocorrelated. This means that the number of observations (sample size) is not a good estimate of the degree of freedom of the model. The p-values computed with use of N^* , however, have not improved the result.

The null hypothesis - that the data on the histogram come from a Beta distribution - was thus rejected regardless of how well a curve fit the histogram visually.

Fig. 5 depicts a series of kernel density estimates, calculated from the I histograms of all analyzed calving events.

Although individual calving I distributions show considerable dispersion, the center of mass of the distributions can be seen to gradually shift towards larger I values as the cliff face ages following calving, i.e. as t_{LC} increases. The peaks of the oldest events, represented by orange and yellow lines, move again towards the middle of the graph. It shows that aging of ice surface causes an observable change in overall reflection intensity that can be tracked using peak-related statistics.

Shapes of certain curves on Fig. 5 reveal another argument against Beta PDF as approximation of I distribution. While most of them retain simple, unimodal shapes there are distributions exhibiting two modes, without an apparent relation between t_{LC} and evolution of the shape. This fact may lie behind the poor performance of the mode of histogram as a I averaging method in the model fitting attempts. Moreover, the bimodality could serve as an argument to reject the Beta function as a model of I values distribution within a contour of a calving event, as the

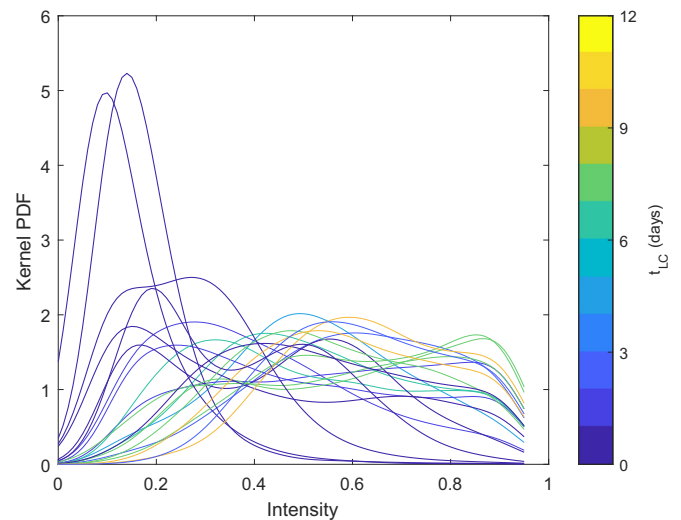


Fig. 5. Kernel density estimation curves created from I histograms of analyzed calving events. Colors indicate t_{LC} of the histogram, which served as a base for a particular curve. (For interpretation of the references to color in this figure legend, the reader is referred to the web version of this article.)

Beta PDF is unimodal (Gupta and Nadarajah, 2004).

3.2. Relationship between I and calving polygon size

Fig. 6A depicts how mean I is distributed depending on the size (surface area) of the calving contour. A vertical cluster of points smaller than 100 m^2 is visible, having very big range of mean intensities. No trend would be reliably found within the group because of the high variability of its mean intensities. It was thus decided to exclude this subset of datapoints from further processing. A test was conducted to determine a size threshold. Only calving contours bigger than the threshold were used for model fitting. Panel B of Fig. 6 shows how the threshold value impacted the GoF of the model to mean I - t_{LC} pairs. Based on it 100 m^2 was chosen as the minimal size for including an event. It is the level at which the coefficient of determination is high

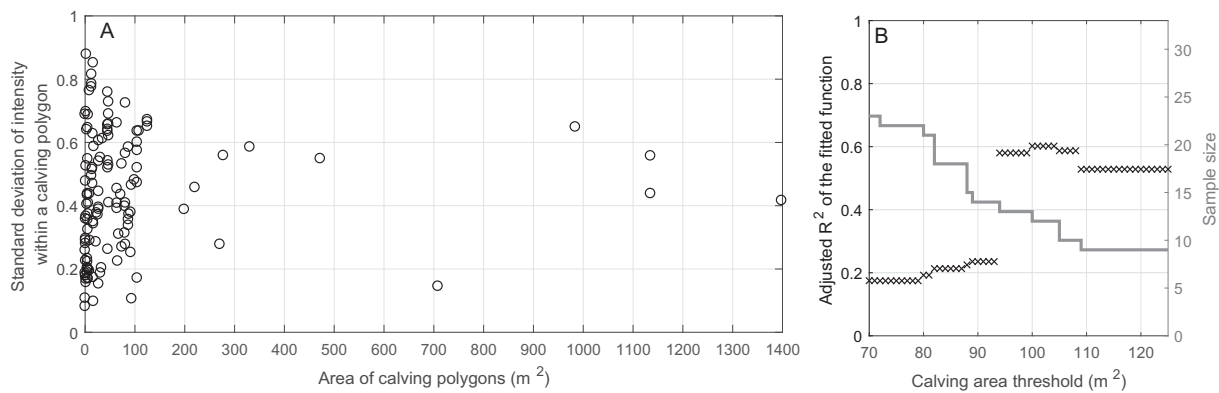


Fig. 6. A: Relationship between mean intensity and size of a calving event. Data points included in the cluster of small events with large variability of mean intensities were discarded from model-fitting procedures. B: Goodness of fit of a model depends on a subset of data points used for fitting. The graph depicts how the R^2 value of an exponential models fitted to mean $I - t_{LC}$ data set varied with choice of different size thresholds. The gray line, with corresponding gray (right) y-axis shows number of calving events used to fit with respective size thresholds imposed.

and the size of sample to which the model is fitted is big enough to ensure quality of results. It is also a value, which corresponds to the right limit of the cluster on Fig. 6A, thus confirming the detrimental impact of the small contours on the model quality.

The large diversity of values found in small calving contours can be seen as a consequence of the cropping of the contours of calving scars. When two calving events overlap, a part of the older one is “refreshed” by the removal of ice by the newer. Thus the surface area of sections of the ice wall corresponding to the older calving gradually decreases. The process results in appearance of many small polygons, representing only small fractions of the whole calving scars, often located close to the scar’s edges. These small contours are unrepresentative for a calving scar in general, as they only include a small part of a section of ice revealed by a calving event. Although the properties of ice enclosed by these small contours are probably more consistent, than when bigger ones are considered, they are not suitable for timing of calving events.

3.3. Determination of ice aging model

The function (Eq. (4)) was fitted to sets of points created with use of each of the four chosen measures of central tendency by means of non-linear regression. Adjusted R^2 was used to assess the goodness of fit of the model to the data. The measure is the ordinary R-squared coefficient of determination with an adjustment term which takes into account the number of fitted coefficients within the model. Fig. 7 depicts the fitted functions and datapoints used for model training. Error bars indicate spatial standard deviation of intensity values for points within each calving polygon and SEM.

The exponential trend of the model is visible in almost all cases. The most significant change of intensity with time occurs within 2 to 4 days from a calving event, in the rapidly rising part of the model function. Regardless of the measure used, many calving events with high t_{LC} are located close to the horizontal “tail” of the function, oscillating around its limit. The numerous “later” points, although fitting the model well, do not provide information on the reflectivity change with time, but only confirm position of the function limit. This may lead to a positive bias when GoF is assessed. Therefore another model fitting attempt was made with only calving events with $t_{LC} < 4$ included. The right column (panels E–H) of Fig. 7 show the result of this fitting. Overall, after the dataset reduction, the adjusted R^2 scores have decreased by about 0.1, confirming the bias introduced by the high- t_{LC} points. In the panel G the more limited dataset led to a better fit. This case, however, is the statistical measure (mode of histogram of I), whose goodness of fit is consistently the worst of all tested.

In both columns of Fig. 7 the mode of fitted Beta functions exhibit highest adjusted R^2 , notably not decreasing with rejection of the “late”

points. It was, however, discussed that the Beta PDF is not a suitable approximation of the distribution of the intensity within calving polygons. Although the fit of the models is good, the datapoints in these cases do not necessarily represent the actual tendency of I .

A difference between median and mean I goodness of fit has appeared after reduction of the dataset, giving an advantage to the latter, indicating that the median might be a better parameter to assess overall reflection intensity within a calving contour, than the mean. Therefore the models fitted to the median I were chosen for prediction efforts. Additionally, the function in panel G was tested for its prediction performance.

Eq.(11) describes the curve presented in Fig. 7F.

$$I = 0.4427 \cdot \exp(-0.3923/t_{LC}) + 0.1685 \quad (11)$$

3.4. Verification of the model

The results of the 5-fold CV and Nash-Sutcliffe indicator values are shown on Fig. 8. The rows demonstrate, respectively, performance of model fitted to median I and all calving contours, median I and calving contours with $t_{LC} > 4$ days and mode of Beta PDF fitted to calving contours with $t_{LC} > 4$ days. Three tests were performed in all cases: verification of datapoints coming from the whole dataset (right column), limited to 4 and 1 day of t_{LC} (middle and left column, respectively).

It can be seen that training the model exclusively on calving events located in the steep section of the model function (i.e. those with $t_{LC} < 4$) improves prediction efficiency regardless of the subset of data used for assessment. The most efficient methods of prediction are those seen on panels E and H: the cases in which the model was trained on early calving events only and an attempt to date events corresponding to the training datasets was made. The E value is negative in nearly all cases shown in the first row of graphs (Fig. 8 A–C), and positive on 3 out of 6 experiments seen in the lower rows. The E coefficient takes values between $-\infty$ and 1, with negative scores indicating that the accuracy of the models is worse than the prediction accuracy obtained when using the mean value of the observations as sole predictor (Moriassi et al., 2007). The last parameter depicted on the figure is RMSE. The root mean square error of predicted values ranges between 3.40 and 0.37 days.

The two graphs depicting the most efficient cases have RMSE of 0.65 and 0.48. This translates into < 16 h and < 12 h of error of assessment of a calving event time with the range of values between 0 and 4 days. The figure demonstrates that presence of $I - t_{LC}$ pairs of “old” calving footprints ($t_{LC} > 4$ days) is hindering prediction effort, even though the GoF of the model fitted to the larger dataset is better than in

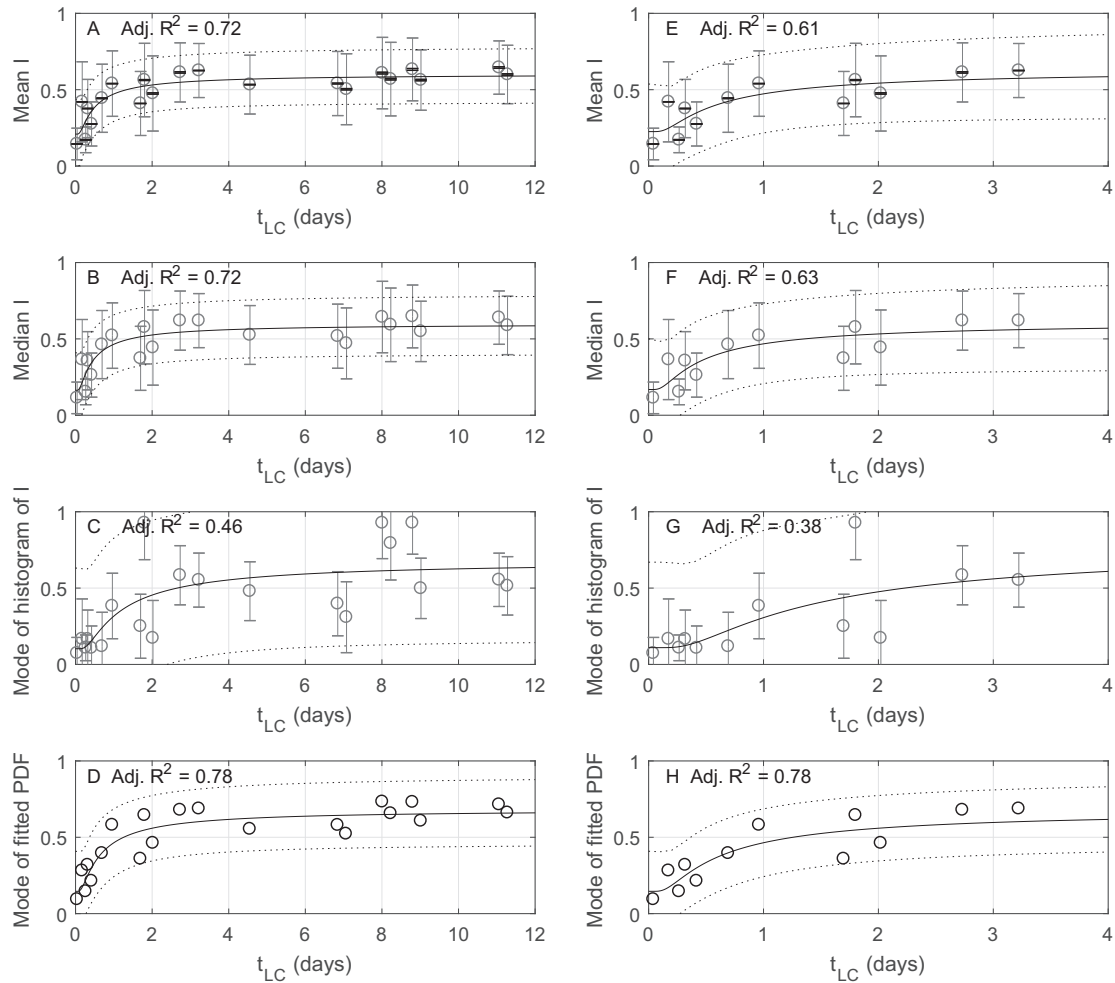


Fig. 7. Relationship between t_{LC} and several measures of I within a calving polygon. Error bars indicate spatial standard deviation of I (gray) and SEM (black, shorter). Black lines are fitted models ($I = a \cdot \exp(b/t_{LC}) + c$, Eq. (11)), dotted lines represent 95% confidence function prediction bounds. The left column (panels A–D) shows results of fitting the model to the full dataset of calving contours bigger than 100 m^2 , while the right (E–H) includes only events with $t_{LC} < 4$ days. Labels of Y axes of graphs indicate which statistical measure was used to produce respective datasets.

case of the more limited collection of points (Fig. 7).

The third row differs from the first two in the dataset used to fit the data: instead of median I , mode of Beta PDF was used. Again a scenario of fitting and verifying the model on young calving polygons only (panel B) yields best results. Both R^2 and E are higher, than when median I is considered. This is in line with better fit of the model to data, as seen on Fig. 7.

4. Discussion

4.1. Geometric uncertainty

In a study dealing with a spatially variable phenomenon, errors arising from an imperfect overlap of analyzed datasets should be discussed. In TLS, factors such as the size of the laser footprint on the target and point density influence the precision of the georegistration of point clouds (Barbarella et al., 2017), as well as issues of the scanning instrument setup, such as leveling and centering (Lichti and Gordon, 2004). Full uncertainty budget analysis was not performed during the study. An assessment of the sensitivity of the final result (the GoF of the $I - t_{LC}$ model) to quality of point cloud coregistration was done by running the model-fitting workflow over datasets with deliberately introduced, random shift between point clouds and calving polygons. The point clouds were moved in the X and Y directions. The distance of displacement was determined randomly from one of two ranges of

values. One of them represented a shift of a magnitude comparable to the magnitude of coregistration RMSE (see Table 1), between 0.5 and 1 m, while the other simulated a large misregistration (between 3 and 5 m). The one-term exponential model was fitted to the datapoints obtained from the transformed data. Table 2 presents the adjusted R-squared coefficient of the different scenarios.

As can be seen in the Table 2, misregistration of clouds or polygon contours impacts the quality of fit significantly. With one exception, the R^2 increases with increasing misplacement of the data. A possible explanation of this trend is mixing of freshly exposed and reworked ice within misplaced calving contours. Translation of calving contours or point clouds by several meters causes them to encompass a portion of white ice, with reflectivity close to I_f , adjacent to the blue ice of calving scars. This leads to higher reflectivities thus causing more datapoints to lie in the part of the model close to the function limit - the same, which introduced a positive bias when fitting. As the misregistration increases, the percentage of points from outside calving scars increases and the effect becomes greater. Fig. 9 shows the boxplots of median I in all cases considered in the Table 2.

The median of medians of I is higher in almost all misregistered cases, than in the situation of correct overlaps. The only exception is case A (with lightly moved point clouds) which is also the only case in which the adj. R^2 has decreased with regard to the correct data. The higher median indicate greater prevalence of higher values of median I , despite relatively unchanged value distribution (although the top walls

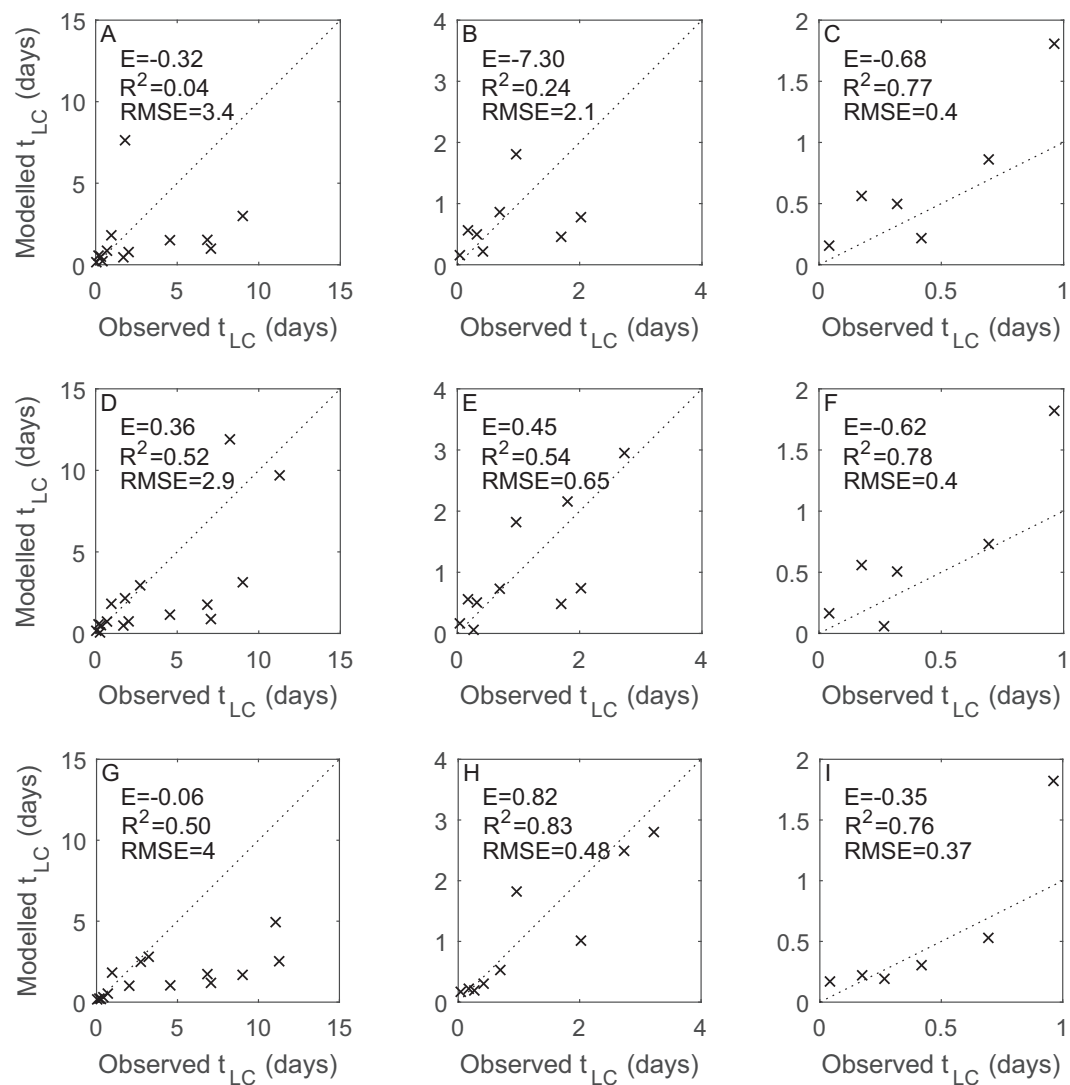


Fig. 8. Predictive performance of the exponential models based on 5-fold cross-validation. All panels show the relationship between modeled and observed t_{LC} with corresponding coefficient of determination (R^2), Nash-Sutcliffe coefficient (E) and RMSE (in days). The columns differ in the sample subset used for plotting and calculation of R^2 and E parameters: The first column (A, D, G) includes all calving events, the second (B, E, H) and third (C, F, I) include only calving events with t_{LC} lower than, respectively, 4 and 1 day. The first row (A–C) contains results for median of $I - t_{LC}$ pairs and the whole set of calving contours larger than 100 m^2 , the second (D–F) adds a $t_{LC} < 4$ constraint to the training data and the third (G–I) uses mode of Beta PDF- I pairs and the same subset as the second. Dotted lines show $x = y$ functions.

Table 2
Adjusted R^2 of the exponential model fitted to datapoints based on various misregistered data and the unchanged dataset (the last column).

Option	Point clouds shifted		Calving polygons shifted		No shift
	0.5–1 m	3–5 m	0.5–1 m	3–5 m	
Case symbol	A	B	C	D	E
Adjusted R^2 (size threshold 100 m^2)	0.60	0.71	0.65	0.72	0.61
Size threshold of the best R^2 (m^2)	100	94	100	105	105
Highest adj. R^2	0.60	0.72	0.65	0.72	0.62

of the boxes A, B, C and D also lie higher, than the top wall of the box E). This may stem from aggregation of, generally brighter, points surrounding the calving scar into the median I in agreement with the hypothesis stated above.

4.2. Prediction efficiency

Fig. 8 shows that the dataset limited to the earliest calving events ($T_{LC} < 4$ days) performs significantly better in predicting t_{LC} from I values than the full dataset. The reason for this discrepancy may reside in the shape of the exponential model. Two regions are seen on the exponential curves of Fig. 7: one with a sharp intensity rise in the area up to 1.5 days of t_{LC} and second, an almost horizontal line beyond t_{LC} of 4 days. The introduction of data points lying in the second part of the curve did increase the GoF, as measured with the adjusted R^2 , but had a detrimental effect on predictions. The $I - t_{LC}$ pairs of these events are scattered above and below the model's limiting value, in inconsistency. In an exponential function like the ones used, even small divergence of observed intensity from the modeled value leads to large error of prediction, as the low-intensity values correspond only to low t_{LC} s and are interpreted as such by the model even despite being found within much older calvings. On the other hand, intensities higher than the limit of the model function find no representation in the model, regardless of the t_{LC} of their corresponding calving events. They were

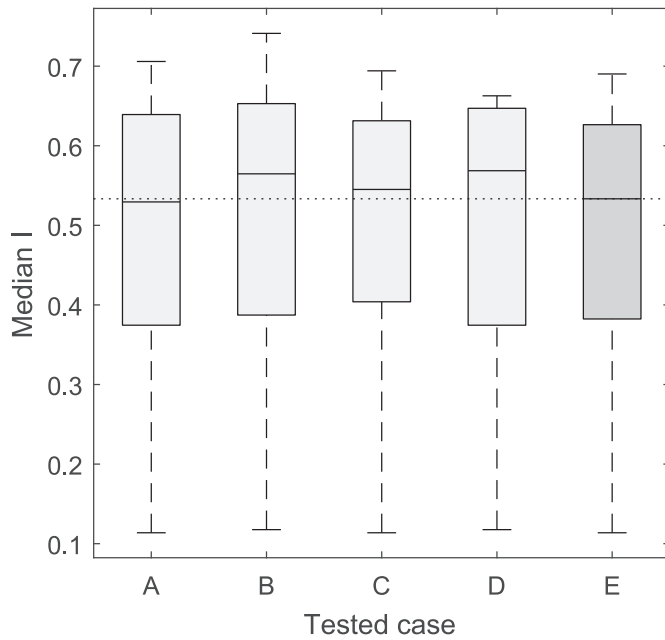


Fig. 9. Boxplots of datasets to which models were fitted which yielded the results described in the third row of Table 2. Letters correspond to the particular misregistration cases (A–D) and correctly registered data (E). The dotted line indicates median of medians of I of the case E.

excluded from validation effort in this study, but in practice this feature of the model would mean that calving events resulting in sufficiently bright scars are impossible to date.

The large deviation of intensity values within each calving polygon may also be a source of error, hindering time prediction. The median intensity was used as the best overall measure of the reflection of a calving event, but the significant dispersion of intensities within each calving footprint, as well as the asymmetrical nature of the distributions, suggests that the whole area exposed by a calving event cannot be considered as a uniform surface.

A number of factors can influence the reflectivity of ice whose interplay may lead to the large diversity of reflection intensities within single calving polygons. These factors are discussed in the following section.

4.3. Physical properties of studied ice

The model interpretation presented in Eq. (5) allows to infer about physical properties of the Fuerza Aerea glacier's ice. The reflectivity of freshly exposed ice in the scanner's wavelength is equal to the model's intercept, that is the parameter c of Eq. (4).

The reflectivity of the ice cliff after reworking can in turn be calculated as the limit of the mathematical function describing the $I - t_{LC}$ relationship. In case of the model investigated here, the limits assume the following form:

$$\lim_{t_{LC} \rightarrow \infty} \left(a \cdot \exp \frac{b}{t_{LC}} + c \right) = a + c \quad (12)$$

Eq.(11) grants values of $I_n = 0.2210$ and $I_f = 0.6304$. The t_{LC} corresponding to I_f is ∞ . It is a consequence of the asymptotic characteristic of the exponential model. The limit of the function, interpreted as the I_f , will only be reached in infinite time. The intensity of 90% of final intensity is reached by the model after 2.65 days, indicating how rapid the rise is in the early t_{LC} s. Very little change of intensity occurs after the model leaves this part of the curve. The difference in intensity over two days between 4 ($I = 0.5874$) and 6 days of t_{LC} ($I = 0.6012$) is comparable to the difference between I of $t_{LC} = 6$ days and the I_f . This

indicates that dating of a calving event with these models would not be possible after 4–6 days since it occurs. The limiting time, however, is probably dependent on the instrument, as each scanner might have different properties such as radiometric resolution, precision of intensity registration, optics and robustness of atmospheric correction algorithms (Calders et al., 2017).

The time at which an ice surface changes its reflectivity from I_n to I_f could be treated as a proxy for weathering rate. In case of Fuerza Aerea the freshly exposed ice surface is made indistinguishable from the ice cliff at large in < 3 days under the conditions of polar summer. This value is a limit of applicability of the model for inference of calving event time with the model. This means that, should a calving event be detected on two subsequent point clouds e.g. by geometric difference, its dating is only possible if the time interval between the two scans is smaller than the time difference between the two modeled values.

Old glacial ice has different optical properties compared to reworked ice, due to long periods of accumulation, refreezing and pressure removing air bubbles from the ice (Benn and Evans, 2014). In such medium which is denser and more uniform than firn or snow, absorption of non-blue wavelengths, is more pronounced than in case of white, more rough ice (Benn and Evans, 2014). The increase of reflectivity with time can be interpreted as gradual introduction of imperfections to the ice surface by subaerial weathering. A section of old ice, once exposed by a calving event, is subject to freeze-thaw cycles and precipitation that alter both its roughness and optical properties. The rate of reflectivity change, or weathering rate, is fastest immediately after a calving event. As processes such as superficial ice melt and refreezing continue and cracks appear in the smooth ice, the surface area of low-reflectivity ice decreases and thickness of newly formed ice increases. After a sufficiently long time further weathering has no influence on reflectivity - a layer of white ice is formed, protecting the deeper ice from the elements. The non-linear, exponential shape of the model indicate that the bulk of the transformation occurs quickly, shortly after a calving event. Surface reflectivity and roughness are among the most prominent factors influencing LiDAR returns (Kashani et al., 2015). Further research would be needed to establish which of these two properties of ice surface, both influenced by subaerial weathering, plays a more important role in the overall reflectivity change.

The increase of reflectivity with time is contrary to the established trend of general “brightening” of ice or snow with age (Cuffey and Paterson, 2010). The interpretation of the results with a formation of new, or reworked, layer of ice on an exposed calving scar can explain this seeming paradox. Weathering crust is a species of ice formed when solar radiation causes subsurface melt and modification of structure of clear ice (Cook et al., 2016b; Müller and Keeler, 1969). Surface smoothness and lack of dispersing media in form of air bubbles are responsible for glacial ice's blue color and increased attenuation of radiation. Compared to blue ice, the weathering crust is more opaque and richer in air (Müller and Keeler, 1969). These features make the surface better at reflecting incoming radiation, including laser beam. The optical properties (including albedo) of weathering crust were not studied in detail. It was proposed that cryoconites can concentrate in the pores of the weathered ice and influence locally melting of ice because of their low albedo (Bøggild et al., 2010; Cooper et al., 2017). This mechanism, however, implies decrease of albedo with time and thus cannot explain the process studied here. Jonsell et al. (2003) have speculated that development and evolution of weathering crust is responsible for daily albedo changes at Storglaciären in Sweden. It was also shown that the layer is sensitive to short-term weather patterns (Cooper et al., 2017). These two clues fit the results of this study, the change of reflectivity of blue ice within a few days.

On a vertical wall of ice protrusions and holes can also be expected to influence deposition of snow and differentiate intensity of insolation which causes the internal melt. Spatial variability of these conditions may lead to non-uniform formation of weathering crust and thus spatially varying reflectivity change rates across a single calving scar. This

would result in the large I range over calving contours observed on Fig. 4 as well as high variability of mean I of small calving contours, encompassing smaller area, with more uniform properties.

4.4. Other uncertainty sources

With the coefficient of determination at 0.63 there remains a share of intensity variability unaccounted for by the processes proposed above. A number of mechanisms, both related to target's properties and data acquisition circumstances, is proposed to explain this.

Liquid water effectively absorbs infrared radiation (Baldrige et al., 2009). On a LiDAR point cloud a highly-absorbing area yield points with zero return intensity, or non-existent. This can be a source of bias which, however, could not be removed, as it affected the studied surface. In the point clouds areas of the cliff close to the sea surface appeared darker (had lower reflection intensity) than the higher parts. It is possible that the wave action sprayed the ice with a thin layer of water which was kept from freezing by salinity or air temperature over 0 °C. Similarly, water contained within snowpack may be problematic for infra-red laser scanning, influencing the scanner range and decreasing the intensity of the returned beam (Deems et al., 2013). The ILRIS-LR instrument used in the present study has been specifically adapted for snow and ice surveys. Reliable range for targets of 10% reflectivity was reported at over 1000 m (OPTECH, 2010). The returns we have obtained from wet, highly absorbing, surfaces can be treated as reliable, as the scanning distance during the fieldwork was below the 1 km range. However, the differences in the degree of surface wetness across the ice cliff may have contributed to the high standard deviation of intensity values observed. Additionally, the factors which rework the glacial surface may also cause the ice wetness to change during the time between laser scans. The same area with slightly more or less moisture may produce a different median intensity than a day earlier, even if a calving event has occurred there long time ago.

The second possible factor is the temperature of the scanning device. It has been shown that for certain laser scanners a correction for the temperature improves the quality of intensity data (Errington and Daku, 2017). The effect however was shown to vary strongly between laser scanner models, becoming insignificant for certain devices. In this study such correction was not performed, as necessary information about the scanner's state during the measurement campaign was unavailable.

Another factor related more to the peculiarities of measurement technique, than to properties of the surface is highlight effect. Described by Tan and Cheng (2017), it appears when a laser beam hits a specular surface at sufficiently low (under 45°) angle. The light reflected and registered by the scanner in such situation is a combination of diffuse reflection and direct, specular, reflection. The latter inflates the reflection intensity value when compared to points hit by laser at higher angles - when only diffuse reflection is recorded. The influence of highlight is particularly high when smooth or reflective surfaces are scanned. Very glassy ice, with very low roughness, can be considered specular surface. On the other hand, more irregular, reworked, ice surface will act as a diffuse reflector, reflecting the incident ray in many directions (Heritage and Large, 2009). The difference could be treated as a material property of the target and counted as one of the processes resulting in ice reflectivity change if not for the highlight effect. The magnitude of specular reflection depends on incidence angle and disappears over 45° in specular surfaces. The reflection mechanism (specular/diffuse) is thus dependent on both surface roughness and, in case of sufficiently smooth targets, incidence angle. This irregularity is not accounted for in the correction Eq. (1). A methodology allowing for correcting for this effect was developed by Tan and Cheng (2017). It relies on scanning a surface of known reflectivity at different angles to determine the relationship between incidence angle and highlight effect. The setup of the fieldwork did not allow for scanning of Fuerza Aerea at different angles, making the data unsuitable for such effort.

The multitude of factors affecting the TLS reflection intensity contributes to big range of I values within calving contours. It is most visible on Fig. 4 and, in form of large spatial standard deviations, on Fig. 7. It can also explain the secondary modes of PDFs seen on Fig. 5. It was not possible to determine, whether the bimodal curves form as a consequence of ice evolution or in response to external influences. Small calving events on top of bigger ones or localized specular reflections could result in a complex distribution of intensities, with a peak of points brighter, or darker, than the general median.

5. Conclusions

Our research has proven successful in determining the relationship between the time of ice exposition and the laser reflection intensity from the surface of an ice cliff. A formula linking mean intensity within a calving scar footprint with the time elapsed since the event in the form of $I = a \exp(b/t_{LC}) + c$ was found to explain the relationship with best efficiency. The coefficient of determination at 0.63 is satisfactory, particularly considering the high dispersion of intensity values within each calving event footprint. Freshly exposed ice surfaces are reworked to a state indistinguishable from older parts of an ice cliff within 3–4 days. The developed model shows that ice aging as seen by surface reflectivity follows an exponential decay law in the form inverse to that of snow (Oerlemans and Knap, 1998). The reflectivity at 1064 nm wavelength rises from 0.22 to 0.63, showing continuous brightening of the ice surface with aging. Processes of subaerial weathering are hypothesized to be the major cause of the change, as they influence the properties of ice (color and roughness) most important for LiDAR reflectivity. Solar radiation can lead to internal melting of the blue ice and formation of porous weathering crust over a calving scar.

Median I and mode of Beta PDF fitted to histogram of I are shown to be the best approximations of central tendency of I within a calving scar. The mode of Beta PDF provides better, than median, fit of the model to the data and performs better in validation. There are, however, arguments against its validity as representation of generalized reflection intensity. The quality of fit of the Beta PDF to intensity data varies due to variations in shape of intensity histogram. In certain cases Beta can be considered invalid, as the histograms exhibit two peaks. This inconsistency, as well as the share of variability of reflectivity not explained by the fitted models, can be caused by factors which impact the quality of LiDAR returns and which could not be eliminated in this study, such as highlight effects and surface wetness of ice. Median of I is to a lesser degree troubled by these problems, but its efficiency is smaller. Nevertheless, the Beta has proven to be a good way to track the shifting center of mass of the I distribution in response to surface aging. Its form, however, fails to fully simulate complexity of I change at the glacial front.

The possibility to determine t_{LC} of a particular part of an ice wall from its generalized I as only input may find use during future LiDAR surveys of calving ice fronts as a method to assess the timing of calving events, expanding the usability of the point clouds. Two possible drawbacks of this approach are 1) the prior necessity of developing a mathematical model from known times and median I s of a set of calving events. Such model, however, once created would be valid for the particular glacier surveyed with the particular scanner. 2) The relatively short temporal limit of applicability. Time intervals between scans during LiDAR measurement campaigns can be sometimes longer, than the 3 days prediction limit highlighted in this study. A calving event detected otherwise and shown to have its median I longer, than the 3 days will not be possible to date.

The latter stems from exponential form of the relationship. The rise of reflectivity is fastest in the 0–3 days of t_{LC} , after which the function flattens and approaches a limit in infinity. The exact formulation of the model, as well as the I_n and I_f values derived from it, are only relevant for Fuerza Aerea glacier scanned with the Optech ILRIS-3D LiDAR scanner. Further work, with more diverse devices and on more ice

fronts, is needed to make attempts at establishing a more universal connection between age of ice surface and reflection intensity. This work provides the foundation for future efforts in this direction.

Recent advances in LiDAR technology grant space for improvement of the model and effectiveness of glacier calving timing predictions. More accurate reflection intensity measurements could eliminate some of the uncertainty sources (such as temperature dependence), or provide more consistent returns from uniform surfaces, reducing the dispersion of intensity returns and making it easier to estimate the most typical reflectivity value of the calved face. Additionally, more information on the scanned surface, such as reflectivities in red, green and blue bands recorded by a scanner's integrated camera, could also serve to build a multispectral model of reflectivity, further improving its quality.

Author contributions

JP did all data processing, majority of calculations and manuscript writing. MP designed the study, formulated time-intensity model and contributed significantly to data analysis and text writing. CK helped in the interpretation of results, data analysis and editing of the manuscript. MP and CK provided the data. All authors contributed to the final manuscript.

Conflict of interests

The authors declare no conflict of interest. The founding sponsors had no role in the design of the study; in the collection, analyses, or interpretation of data; in the writing of the manuscript, and in the decision to publish the results.

Acknowledgments

We thank Sandro Zambra for the processing of video data, Jakob Abermann and the staff of Chilean Navy Antarctic Base Arturo Prat for support in data collection. This study was funded by the Chilean National Antarctic Institute (INACH) grant RT_12-12 and, within statutory activities, Grant No. 3841/E-41/S/2017 of the Ministry of Science and Higher Education of Poland. MP was partially supported by CECs, funded by the Centers of Excellence Base Financing Program of the Comisión Nacional de Investigación Científica y Tecnológica (CONICYT-Chile). CK is funded by the Natural Sciences and Engineering Research Council of Canada grant RGPIN-2015-03844. We also thank the reviewers of the first manuscript of this article. Their comments have had a significant, positive impact on the article.

References

- Anderson, T.W., Darling, D.A., 1954. A test of goodness of fit. *J. Am. Stat. Assoc.* 49 (268), 765–769.
- Baldrige, A., Hook, S., Grove, C., Rivera, G., 2009. The ASTER spectral library version 2.0. *Remote Sens. Environ.* 113 (4), 711–715.
- Barbarella, M., Fiani, M., Lugli, A., 2017. Uncertainty in terrestrial laser scanner surveys of landslides. *Remote Sens.* 9 (2), 113.
- Bender, N.A., Crosbie, K., Lynch, H.J., 2016. Patterns of tourism in the Antarctic Peninsula region: a 20-year analysis. *Antarct. Sci.* 28 (03), 194–203.
- Benn, D., Evans, D.J., 2014. *Glaciers and Glaciation*. Routledge.
- Bhardwaj, A., Sam, L., Bhardwaj, A., Martin-Torres, F., 2016. LiDAR remote sensing of the cryosphere: present applications and future prospects. *Remote Sens. Environ.* 177, 125–143.
- Bliss, A., Cogley, G., Frank, P., Le Bris, R., Berthier, E., 2014. GLIMS Glacier Database. Bøggild, C.E., Brandt, R.E., Brown, K.J., Warren, S.G., 2010. The ablation zone in northeast Greenland: ice types, albedos and impurities. *J. Glaciol.* 56 (195), 101–113.
- Calders, K., Disney, M.I., Armston, J., Burt, A., Brede, B., Origo, N., Muir, J., Nightingale, J., 2017. Evaluation of the range accuracy and the radiometric calibration of multiple terrestrial laser scanning instruments for data interoperability. *IEEE Trans. Geosci. Remote Sens.* 55 (5), 2716–2724.
- Carrivick, J.L., Geilhausen, M., Warburton, J., Dickson, N.E., Carver, S.J., Evans, A.J., Brown, L.E., 2013. Contemporary geomorphological activity throughout the proglacial area of an Alpine catchment. *Geomorphology* 188, 83–95.
- CloudCompare, 2017. Cloudcompare (Version 2.9) [gpl software]. <http://www.cloudcompare.org/>.
- Cook, A., Fox, A., Vaughan, D., Ferrigno, J., 2005. Retreating glacier fronts on the Antarctic Peninsula over the past half-century. *Science* 308 (5721), 541–544.
- Cook, A., Holland, P., Meredith, M., Murray, T., Luckman, A., Vaughan, D., 2016a. Ocean forcing of glacier retreat in the western Antarctic Peninsula. *Science* 353 (6296), 283–286.
- Cook, J.M., Hodson, A.J., Irvine-Fynn, T.D., 2016b. Supraglacial weathering crust dynamics inferred from cryoconite hole hydrology. *Hydrol. Process.* 30 (3), 433–446.
- Cooper, M.G., Smith, L.C., Rennermalm, A.K., Miège, C., Pitcher, L.H., Ryan, J.C., Yang, K., Cooley, S., 2017. Near-surface meltwater storage in low density bare ice of the Greenland Ice Sheet ablation zone. *Cryosphere Discuss.* 1–25.
- Cuffey, K.M., Paterson, W.S.B., 2010. *The Physics of Glaciers*. Academic Press.
- Dasgupta, S., Laplante, B., Meisner, C., Wheeler, D., Yan, J., 2009. The impact of sea level rise on developing countries: a comparative analysis. *Clim. Chang.* 93 (3), 379–388.
- De Sanjosé, J., Berenguer, F., Atkinson, A., De Matías, J., Serrano, E., Gómez-Ortiz, A., González-García, M., Rico, I., 2014. Geomatics techniques applied to glaciers, rock glaciers, and ice patches in Spain (1991–2012). *Geogr. Ann.* 96 (3), 307–321.
- Deems, J.S., Painter, T.H., Finnegan, D.C., 2013. Lidar measurement of snow depth: a review. *J. Glaciol.* 59 (215), 467–479.
- Dhargalkar, V., Verlecar, X., 2009. Southern Ocean seaweeds: a resource for exploration in food and drugs. *Aquaculture* 287 (3), 229–242.
- Dowdeswell, J., Benham, T., Strozzi, T., Hagen, J., 2008. Iceberg calving flux and mass balance of the Austfonna ice cap on Nordaustlandet, Svalbard. *J. Geophys. Res. Earth Surf.* 113 (F3).
- Eguiluz, V.M., Fernández-Gracia, J., Irigoien, X., Duarte, C.M., 2016. A quantitative assessment of Arctic shipping in 2010–2014. *Sci. Rep. U. K.* 6.
- Eitel, J.U., Höfle, B., Vierling, L.A., Abellán, A., Asner, G.P., Deems, J.S., Glennie, C.L., Joerg, P.C., LeWinter, A.L., Magney, T.S., et al., 2016. Beyond 3-D: the new spectrum of lidar applications for Earth and ecological sciences. *Remote Sens. Environ.* 186, 372–392.
- Errington, A.F., Daku, B.L., 2017. Temperature compensation for radiometric correction of terrestrial LiDAR intensity data. *Remote Sens.* 9 (4), 356.
- Fang, W., Huang, X., Zhang, F., Li, D., 2015. Intensity correction of terrestrial laser scanning data by estimating laser transmission function. *IEEE Trans. Geosci. Remote Sens.* 53 (2), 942–951.
- Fischer, M., Huss, M., Kummert, M., Hoelzle, M., 2016. Application and validation of long-range terrestrial laser scanning to monitor the mass balance of very small glaciers in the Swiss Alps. *Cryosphere* 10 (3), 1279–1295.
- Fretwell, P., Hodgson, D., Watcham, E., Bentley, M., Roberts, S., 2010. Holocene isostatic uplift of the South Shetland Islands, Antarctic Peninsula, modelled from raised beaches. *Quat. Sci. Rev.* 29 (15), 1880–1893.
- Gabbud, C., Micheletti, N., Lane, S., 2015. Lidar measurement of surface melt for a temperate Alpine glacier at the seasonal and hourly scales. *J. Glaciol.* 61 (229), 963–974.
- Gallay, M., 2012. Direct acquisition of data: airborne laser scanning. In: Cook, S., Clarke, L., Nield, J. (Eds.), *Geomorphological Techniques* (Online Edition). British Society for Geomorphology, London, pp. 1–17.
- Gardner, A.S., Moholdt, G., Cogley, J.G., Wouters, B., Arendt, A.A., Wahr, J., Berthier, E., Hock, R., Pfeffer, W.T., Kaser, G., et al., 2013. A reconciled estimate of glacier contributions to sea level rise: 2003 to 2009. *Science* 340 (6134), 852–857.
- Glowacki, O., Deane, G., Moskalik, M., Blondel, P., Tegowski, J., Blaszczyk, M., 2015. Underwater acoustic signatures of glacier calving. *Geophys. Res. Lett.* 42 (3), 804–812.
- Griffith, D.A., 2005. Effective geographic sample size in the presence of spatial autocorrelation. *Ann. Assoc. Am. Geogr.* 95 (4), 740–760.
- Gross, H., Jutzi, B., Thoennessen, U., 2008. Intensity normalization by incidence angle and range of full-waveform lidar data. *Int. Soc. Photogramm.* 37, 405–412.
- Gupta, A.K., 2011. Beta distribution. In: Lovric, M. (Ed.), *International Encyclopedia of Statistical Science*. Springer, Berlin, Heidelberg, pp. 144–145.
- Gupta, A.K., Nadarajah, S., 2004. *Handbook of Beta Distribution and Its Applications*. Marcel Dekker.
- Hall, B., 2010. Holocene relative sea-level changes and ice fluctuations in the South Shetland Islands. *Glob. Planet. Chang.* 74 (1), 15–26.
- Harpold, A.A., Marshall, J.A., Lyon, S.W., Barnhart, T.B., Fisher, B., Donovan, M., Brubaker, K.M., Crosby, C.J., Glenn, N.F., Glennie, C.L., et al., 2015. Laser vision: lidar as a transformative tool to advance critical zone science. *Hydrol. Earth Syst. Sci.* 19, 2881–2897.
- Heritage, G.L., Large, A.R., 2009. Principles of 3D laser scanning. In: *Laser Scanning for the Environmental Sciences*. Wiley Online Library, pp. 21–34.
- Hock, R., de Woul, M., Radić, V., Dyurgerov, M., 2009. Mountain glaciers and ice caps around Antarctica make a large sea-level rise contribution. *Geophys. Res. Lett.* 36 (7).
- Höfle, B., Geist, T., Rutzinger, M., Pfeifer, N., 2007. Glacier surface segmentation using airborne laser scanning point cloud and intensity data. *Int. Soc. Photogramm.* 36 (Part 3), W52.
- Holland, D., Voytenko, D., Christianson, K., Dixon, T., Mei, J., Parizek, B., Vaňková, I., Walker, R., Walter, J., Nicholls, K., Holland, D., 2016. An intensive observation of calving at Helheim Glacier, East Greenland. *Oceanography* 29 (4), 46–61.
- Hopkinson, C., Barlow, J., Demuth, M., Pomeroy, J., 2010. Mapping changing temperature patterns over a glacial moraine using oblique thermal imagery and lidar. *Can. J. Remote Sens.* 36 (sup2), S257–S265.
- Hopkinson, C., Collins, T., Anderson, A., Pomeroy, J., Spooner, I., 2012. Spatial snow depth assessment using LiDAR transect samples and public GIS data layers in the Elbow River watershed, Alberta. *Can. Water. Resour. J.* 37 (2), 69–87.
- Hopkinson, C., Demuth, M., Sitar, M., Chasmer, L., 2001. Applications of airborne LiDAR mapping in glacierised mountainous terrain. In: *Geoscience and Remote Sensing Symposium, 2001. IGARSS'01. IEEE 2001 International. vol. 2. IEEE*, pp. 949–951.

- Jóhannesson, T., Björnsson, H., Magnússon, E., Guðmundsson, S., Pálsson, F., Sigurðsson, O., Thorsteinsson, T., Berthier, E., 2013. Ice-volume changes, bias estimation of mass-balance measurements and changes in subglacial lakes derived by lidar mapping of the surface of Icelandic glaciers. *Ann. Glaciol.* 54 (63), 63–74.
- Jonsell, U., Hock, R., Holmgren, B., 2003. Spatial and temporal variations in albedo on Storglaciären, Sweden. *J. Glaciol.* 49 (164), 59–68.
- Kääb, A., Berthier, E., Nuth, C., Gardelle, J., Arnaud, Y., 2012. Contrasting patterns of early twenty-first-century glacier mass change in the Himalayas. *Nature* 488 (7412), 495–498. <http://dx.doi.org/10.1038/nature11324>.
- Kaasalainen, S., Jaakkola, A., Kaasalainen, M., Krooks, A., Kukko, A., 2011a. Analysis of incidence angle and distance effects on terrestrial laser scanner intensity: search for correction methods. *Remote Sens.* 3 (10), 2207–2221.
- Kaasalainen, S., Kaartinen, H., Kukko, A., 2008. Snow cover change detection with laser scanning range and brightness measurements. *EARSeL eProc.* 7 (2), 133–141.
- Kaasalainen, S., Pyysalo, U., Krooks, A., Vain, A., Kukko, A., Hyypä, J., Kaasalainen, M., 2011b. Absolute radiometric calibration of ALS intensity data: effects on accuracy and target classification. *Sensors* 11 (11), 10586–10602.
- Kashani, A.G., Olsen, M.J., Parrish, C.E., Wilson, N., 2015. A review of LIDAR radiometric processing: from Ad Hoc intensity correction to rigorous radiometric calibration. *Sensors* 15 (11), 28099–28128.
- Katsman, C.A., Sterl, A., Beersma, J., Van den Brink, H., Church, J., Hazeleger, W., Kopp, R., Kroon, D., Kwadijk, J., Lammersen, R., et al., 2011. Exploring high-end scenarios for local sea level rise to develop flood protection strategies for a low-lying delta - the Netherlands as an example. *Clim. Chang.* 109 (3–4), 617–645.
- Kerkez, B., Glaser, S.D., Bales, R.C., Meadows, M.W., 2012. Design and performance of a wireless sensor network for catchment-scale snow and soil moisture measurements. *Water Resour. Res.* 48 (July 2011), 1–18. <http://dx.doi.org/10.1029/2011WR011214>.
- Kociuba, W., Kubisz, W., Zagórski, P., 2014. Geomorphology Use of terrestrial laser scanning (TLS) for monitoring and modelling of geomorphic processes and phenomena at a small and medium spatial scale in Polar environment (Scott River - Spitsbergen). *Geomorphology* 212, 84–96. <http://dx.doi.org/10.1016/j.geomorph.2013.02.003>.
- Landy, J.C., Komarov, A.S., Barber, D.G., 2015. Numerical and experimental evaluation of terrestrial LiDAR for parameterizing centimeter-scale sea ice surface roughness. *IEEE Trans. Geosci. Remote Sens.* 53 (9), 4887–4898.
- Lasserre, F., Beveridge, L., Fournier, M., Têtu, P.-L., Huang, L., 2016. Polar seaways? Maritime transport in the Arctic: an analysis of shipowners' intentions II. *J. Transp. Geogr.*
- Lichti, D.B., Gordon, S.J., 2004. Error propagation in directly georeferenced terrestrial laser scanner point clouds for cultural heritage recording. In: *Proc. of FIG Working Week, Athens, Greece, May*, pp. 22–27.
- Luckman, A., Benn, D.I., Cottier, F., Bevan, S., Nilsen, F., Inall, M., 2015. Calving rates at tidewater glaciers vary strongly with ocean temperature. *Nat. Commun.* 6.
- Lüthi, M., Vieli, A., 2016. Multi-method observation and analysis of a tsunami caused by glacier calving. *Cryosphere* 10, 995–1002.
- Moeser, D., Stähli, M., Jonas, T., 2015. Improved snow interception modeling using canopy parameters derived from airborne LiDAR data. *Water Resour. Res.* 51, 5041–5059.
- Moriassi, D.N., Arnold, J.G., Van Liew, M.W., Bingner, R.L., Harmel, R.D., Veith, T.L., 2007. Model evaluation guidelines for systematic quantification of accuracy in watershed simulations. *T. ASABE* 50 (3), 885–900.
- Müller, F., Keeler, C.M., 1969. Errors in short-term ablation measurements on melting ice surfaces. *J. Glaciol.* 8 (52), 91–105.
- Nash, J.E., Sutcliffe, J.V., 1970. River flow forecasting through conceptual models part I - a discussion of principles. *J. Hydrol.* 10 (3), 282–290.
- Navarro, F., Jonsell, U., Corcuera, M., Martín-Español, A., 2013. Decelerated mass loss of Hurd and Johnsons Glaciers, Livingston Island, Antarctic Peninsula. *J. Glaciol.* 59 (213), 115–128.
- Oerlemans, J., Knap, W., 1998. A 1 year record of global radiation and albedo in the ablation zone of Morteratschgletscher, Switzerland. *J. Glaciol.* 44 (147), 231–238.
- Oliva, M., Navarro, F., Hrbáček, F., Hernández, A., Nývlt, D., Pereira, P., Ruiz-Fernández, J., Trigo, R., 2017. Recent regional climate cooling on the Antarctic Peninsula and associated impacts on the cryosphere. *Sci. Total Environ.* 580, 210–223.
- OPTECH, 2010. ILRIS Terrestrial Laser Scanner Summary Specification Sheet. Optech Incorporated.
- Petrich, C., Eicken, H., Polashenski, C.M., Sturm, M., Harbeck, J.P., Perovich, D.K., Finnegan, D.C., 2012. Snow dunes: a controlling factor of melt pond distribution on Arctic sea ice. *J. Geophys. Res.* 117, 1–10.
- Pełlicki, M., Kinnard, C., 2016. Calving of Fuerza Aérea Glacier (Greenwich Island, Antarctica) observed with terrestrial laser scanning and continuous video monitoring. *J. Glaciol.* 62 (232), 851–863.
- Pełlicki, M., Sziłó, J., MacDonell, S., Vivero, S., Bialik, R.J., 2017. Recent deceleration of the ice elevation change of ecology glacier (King George Island, Antarctica). *Remote Sens.* 9 (6), 520.
- Raschke, M., 2011. Empirical behaviour of tests for the beta distribution and their application in environmental research. *Stoch. Env. Res. Risk A.* 25 (1), 79–89.
- Rau, F., Mauz, F., Vogt, S., Khalsa, S.J.S., Raup, B., 2005. Illustrated GLIMS Glacier Classification Manual.
- Rignot, E., Jacobs, S., Mouginot, J., Scheuchl, B., 2013. Ice-shelf melting around Antarctica. *Science* 341 (6143), 266–270.
- Roncat, A., Wieser, M., Briesche, C., Bollmann, E., Sailer, R., Klug, C., Pfeifer, N., 2013. Analysing the suitability of radiometrically calibrated full-waveform lidar data for delineating Alpine rock glaciers. *Int. Soc. Photogramm.* 1, 1.
- Ryan, J., Hubbard, A., Box, J., Todd, J., Christoffersen, P., Carr, J., Holt, T., Snooke, N., 2015. UAV photogrammetry and structure from motion to assess calving dynamics at Store Glacier, a large outlet draining the Greenland ice sheet. *Cryosphere* 9 (1), 1–11.
- Sakakibara, D., Sugiyama, S., 2014. Ice-front variations and speed changes of calving glaciers in the Southern Patagonia Icefield from 1984 to 2011. *J. Geophys. Res. Earth Surf.* 119 (11), 2541–2554.
- Schannwell, C., Barrand, N.E., Radić, V., 2016. Future sea-level rise from tidewater and ice-shelf tributary glaciers of the Antarctic Peninsula. *Earth Planet. Sci. Lett.* 453, 161–170.
- Simms, A.R., Ivins, E.R., DeWitt, R., Kouremenos, P., Simkins, L.M., 2012. Timing of the most recent Neoglacial advance and retreat in the South Shetland Islands, Antarctic Peninsula: insights from raised beaches and Holocene uplift rates. *Quat. Sci. Rev.* 47, 41–55.
- Slangen, A., Adloff, F., Jevrejeva, S., Leclercq, P., Marzeion, B., Wada, Y., Winkelmann, R., 2016. A review of recent updates of sea-level projections at global and regional scales. *Surv. Geophys.* 1–22.
- Starek, M., Luzum, B., Kumar, R., Slatton, K., 2006. Normalizing lidar intensities. In: *Tech. rep. Geosensing Engineering and Mapping (GEM) Civil and Coastal Engineering Department University of Florida*.
- Tan, K., Cheng, X., 2017. Specular reflection effects elimination in terrestrial laser scanning intensity data using phong model. *Remote Sens.* 9 (8), 853.
- Tin, T., Fleming, Z.L., Hughes, K.A., Ainley, D., Convey, P., Moreno, C., Pfeiffer, S., Scott, J., Snape, I., 2009. Impacts of local human activities on the Antarctic environment. *Antarct. Sci.* 21 (01), 3–33.
- Turner, J., Lu, H., White, I., King, J.C., Phillips, T., Hosking, J.S., Bracegirdle, T.J., Marshall, G.J., Mulvaney, R., Deb, P., 2016. Absence of 21st century warming on Antarctic Peninsula consistent with natural variability. *Nature* 535 (7612), 411–415.
- van den Broeke, M., Bamber, J., Ettema, J., Rignot, E., Schrama, E., van de Berg, W.J., van Meijgaard, E., Velicogna, I., Wouters, B., 2009. Partitioning recent Greenland mass loss. *Science* 326 (5955), 984–986.
- van den Broeke, M.R., Enderlin, E.M., Howat, I.M., Noël, B.P., 2016. On the recent contribution of the Greenland ice sheet to sea level change. *Cryosphere* 10 (5), 1933.
- Vaughan, D., Comiso, J., Allison, I., Carrasco, J., Kaser, G., Kwok, R., Mote, P., Murray, T., Paul, F., Ren, J., Rignot, E., Solomina, O., Steffen, K., Zhang, T., 2013. Observations: cryosphere. In: *Climate Change 2013: The Physical Science Basis. Contribution of Working Group I to the Fifth Assessment Report of the Intergovernmental Panel on Climate Change*. Cambridge University Press, Cambridge, United Kingdom and New York, NY, USA.
- Vaughan, D., Marshall, G., Connolley, W., Parkinson, C., Mulvaney, R., Hodgson, D., King, J., Pudsay, C., Turner, J., 2003. Recent rapid regional climate warming on the Antarctic Peninsula. *Clim. Chang.* 60 (3), 243–274.
- Xie, S., Dixon, T.H., Voytenko, D., Holland, D.M., Holland, D., Zheng, T., 2016. Precursor motion to iceberg calving at Jakobshavn Isbræ, Greenland, observed with terrestrial radar interferometry. *J. Glaciol.* 62 (236), 1134–1142.